

Acquire Precise and Comparable Fundus Image Quality Score: FTHNet and FQS Dataset

Zheng Gong^{1,*}, Zhuo Deng^{1,*}, Run Gan², Zhiyuan Niu¹, Lu Chen², Canfeng Huang², Jia Liang², Weihao Gao¹, Fang Li¹, Shaochong Zhang^{2,†}, Lan Ma^{1,†}

¹ The Shenzhen International Graduate School, Tsinghua University

² The Shenzhen Eye Hospital

* equal contribution

† corresponding author

Abstract

Objective: The retinal fundus images are utilized extensively in the diagnosis, and their quality can directly affect the diagnosis results. However, due to the insufficient dataset and algorithm application, current fundus image quality assessment (FIQA) methods are not powerful enough to meet ophthalmologists' demands.

Methods: In this paper, we address the limitations of datasets and algorithms in FIQA. First, we establish a new FIQA dataset, Fundus Quality Score(FQS), which includes 2246 fundus images with two labels: a continuous Mean Opinion Score varying from 0 to 100 and a three-level quality label. Then, we propose a FIQA Transformer-based Hypernetwork (FTHNet) to solve these tasks with regression results rather than classification results in conventional FIQA works.

Results: The FTHNet is optimized for the FIQA tasks with extensive experiments. Results on our FQS dataset show that the FTHNet can give quality scores for fundus images with PLCC of 0.9423 and SRCC of 0.9488, significantly outperforming other methods with fewer parameters and less computation complexity.

Conclusion: We successfully build a dataset and model addressing the problems of current FIQA methods. Furthermore, the model deployment experiments demonstrate its potential in automatic medical image quality control.

Significance: All experiments are carried out with 10-fold cross-validation to ensure the significance of the results.

Keywords:

Deep learning, Image Quality Assessment, Retinal Fundus Image, Transformer.

1. Introduction

The retinal fundus image is one of the most commonly used ophthalmology graphics. Many ophthalmologists use fundus images to assist clinical diagnosis of diabetic retinopathy (DR) [1, 2, 3], age-related macular degeneration (AMD) [4], polypoidal choroidal vasculopathy (PCV) [5], and other retinal diseases [6, 7]. The precise diagnosis of eye diseases relies on high-quality(HQ) fundus images. However, fundus images captured with different equipment by ophthalmologists with various levels of experience have large variations in quality. A screening study of 5,575 patients found that about 12% of fundus images are of inadequate quality to be readable by ophthalmologists [8]. Moreover, another study based on UK BioBank also shows that more than 25% of fundus images need to be of higher quality to al-

low accurate diagnosis. Consequently, low-quality(LQ) fundus images cover a significant percentage of clinical fundus images. According to the experience of ophthalmologists, the common degradation types of LQ fundus images include out-of-focus blur, motion blur, artifact, over-exposure, and over-darkness. The degradation of fundus images may prevent a reliable clinical diagnosis by ophthalmologists or computer-aided systems. Thus, fundus image quality assessment (FIQA) is proposed to help ophthalmologists control the quality of fundus images. The FIQA tasks can be bonded with the collection process of fundus images, which can boost its speed and avoid useless repeats. Moreover, the quality control process in the medical record system can also benefit from FIQA methods. Thus, the research in FIQA is important.

Traditional FIQA methods [9, 10, 11] are mainly based on hand-crafted modeling. However, these modeling methods achieve unsatisfactory performance and generality. In recent years, Convolutional Neural Networks (CNNs) have been widely used in image quality assessment (IQA) [12, 13, 14, 15]. Inspired by the success of IQA, CNNs have also been applied to FIQA [16, 17]. Although impressive results have been achieved, CNN-based methods show limitations in capturing long-range dependencies. Recently, the Transformer [18] has been introduced into computer vision and outperformed CNN-based methods in many tasks. The Multi-head Self-Attention (MSA) in the Transformer exhibits excellent performance modeling non-local similarity and long-term dependencies. This advantage of the Transformer may address the limitations of CNN-based models.

Meanwhile, most present FIQA methods are data-driven, which means the performance of these methods relies on the quality of the data. Unfortunately, a professional and available clinical benchmark has yet to be explored. **Firstly**, some datasets [19, 20, 16] treat the FIQA task as a classification task rather than a regression task. The fundus images are roughly divided into several categories, such as “Good”, “Usable”, and “Bad” quality. The roughly labeled images can lead to images of prominently different quality classified in the same category. **Secondly**, when a quality scale is used, some datasets do not consider that the image quality of different fundus regions has different effects on clinical diagnosis. For example, the influence of optic disc regions on the fundus image quality should be more significant than that of edge regions. **Thirdly**, many works train and test on their private datasets, which are labeled using their own standard and are not publicly available. Therefore, it is not convenient to benchmark the performance of the FIQA methods.

In this paper, we set out to address the limitations of algorithms and datasets in FIQA. To begin with, we establish a new clinically acquired dataset, Fundus Quality Scores (FQS), including 2246 fundus images with continuous mean opinion scores (MOSs) ranging from 0 to 100 and three-level labels (“Good”, “Reject”, and “Usable”). Based on this dataset, we propose a novel method for FIQA, namely the FIQA Transformer-based HyperNetwork (FTHNet). The proposed FTHNet consists of four parts: the Transformer Backbone, the Distortion Perception Network, the Parameter Hypernetwork, and the Target Network. Specifically, the Transformer Backbone is built up by Basic Transformer Blocks (BTBs). The self-attention mechanism in BTBs can capture the non-local self-similarity and long-term

dependencies, which are the main limitations of existing CNN-based methods. The proposed Distortion Perception Network can collect distortion information in different resolutions. We introduce the Parameter Hypernetworks, which can dynamically generate weights and biases according to fundus image contents. Furthermore, the Target Network receives the weights and biases and predicts fundus image quality scores. This proposed method is supposed to give prediction scores consistent with ophthalmologists’ experience and perception.

Our contributions can be summarized as follows:

- We establish a new clinical dataset, FQS, to evaluate FIQA algorithms. This is the first professional and available FIQA dataset with both continuous MOSs and three-level classification labels.
- We propose a novel FIQA model with the Transformer-based hypernetwork, FTHNet. It is the first attempt to introduce the Transformer aligning with hypernetwork to FIQA tasks.
- Experimental results demonstrate that our FTHNet significantly outperforms current algorithms in the FIQA tasks with fewer parameters and less computation complexity, and thus has excellent potential in real-time diagnosis assistance.

2. Material and methods

2.1. Fundus Quality Score

This subsection introduces our clinical dataset, Fundus Quality Score (FQS). It contains 2246 fundus images with a spatial size of 2304×1728 . In FQS, each image has two labels, a three-level classification label (good, reject, and usable) and a continuous Mean Opinion Score (MOS) varying from 0 to 100 with a minimum gap of 1.

2.1.1. Data Collecting

We select 2246 fundus images with typical degradation or pathological features from over 10,000 eye instances. Specifically, 92% of selected images are from the usual clinical diagnosis across all ages and genders, and the other 8% are from teens’ myopia screening, which has higher image quality and fewer pathological features. These images can cover most retinal photographing formations of eye hospitals.

The collection process of our FQS is approved and supervised by Shenzhen Eye Hospital. The fundus images are captured by ophthalmologists using a ZEISS

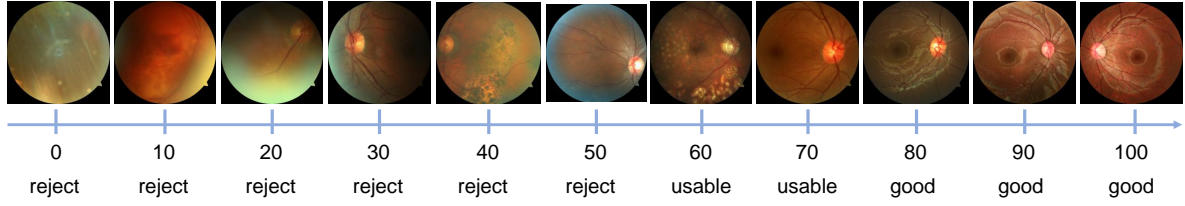


Figure 1: Examples of the Fundus Quality Score (FQS) dataset. In the FQS dataset, each fundus image has two labels: a three-level classification label (good, reject, and usable) and a continuous MOS varying from 0 to 100. Our FQS dataset covers the most common degradation types in clinical diagnoses, such as out-of-focus blur, haze, uneven illumination, and over-darkness.

VISUCAM200 fundus camera or a Canon fundus camera, which are the mainstream products of fundus cameras. Sensitive information, such as names and diagnosis results, is deleted from the beginning of data collection. We also deleted the EXIF metadata of fundus images.

2.1.2. Labelling

In our FQS, we propose a new and complete fundus image quality scale including a three-level classification label (“Good”, “Reject”, and “Usable”) and a continuous MOS varying from 0 to 100 with a minimum gap of 1. An example of the quality scale can be seen in Fig. 1.

Unlike natural IQA, the fundus image quality evaluation needs more professional consideration of the influence of image quality on clinical diagnosis. Therefore, we invite 3 ophthalmologists and design a set of rigorous and scientific labeling processes.

Firstly, we set up the reference set, including 330 fundus images with three-level classification labels (“Good”, “Reject”, and “Usable”) and MOS. The reference set is constructed by an experienced ophthalmologist based on clinical experience. Then, the images in each category are further classified into five levels by their degree of degradation (extent of the out-of-focus blur, haze, uneven illumination, etc.). The scores of these images are further altered by assessing the following questions to determine their final MOSs:

- (1) Whether the degree of fundus image degradation is serious compared to the images in the same category.
- (2) Whether the structural information that fundus images provide (blood vessel shape and quantity) is comprehensive.
- (3) Whether the pathological feature is clear enough for clinical diagnosis.
- (4) Whether the critical position (macula, optic disk, etc.) is visible and clear.

Secondly, three experienced ophthalmologists gave their opinion scores for 2246 images under the guidance of the reference set. In addition, we also invited three other junior ophthalmologists. To make the labeling process more convenient, we built the software Fundus-Marking (shown in Appendix, Fig.A.6). This software has a straightforward GUI and can be easily modified to build any new IQA datasets. Note that scores will be discussed and adjusted if there is a significant difference between the opinion scores of the same image. **Finally**, we obtain the MOS by the weighted average of six independent scores:

$$\text{MOS} = \lambda_1 \sum_{i=1}^3 \mathbf{O}_i + \lambda_2 \sum_{i=1}^3 \mathbf{O}_{j_i}, \quad (1)$$

where \mathbf{O}_i and \mathbf{O}_{j_i} denote the opinion scores of experienced ophthalmologists and junior ophthalmologists. λ_1 and λ_2 represent the weights of junior ophthalmologists and experienced ophthalmologists, which are set to 0.11 and 0.22.

2.1.3. Statistic Information

MOS Distribution Histogram Fig.2 (a) depicts the distribution of MOS. It can be observed that most of the MOSs are distributed between 60 and 80. The number of images with MOS distributed between 70 and 80 is the largest, and the number of images from 90 to 100 is the lowest, with only 15. The MOS distribution in our FQS is natural and consistent with actual clinical experience. Affected by the equipment and patient coordination, it is difficult to obtain very high-quality fundus images (MOS: 80 or above) in actual clinical collecting. Meanwhile, retinal fundus images of extremely low quality are also rare. The quality of most clinical fundus images is in the upper middle of the score scale.

Three-level Label Distribution The distribution of the three-level classification label is shown in Fig.2 (c). Since the HQ images are similar, but the LQ images are different in numerous aspects, there are more “Reject” images in the FQS dataset to cover more degradation types. The numbers of fundus images labeled “Good”,

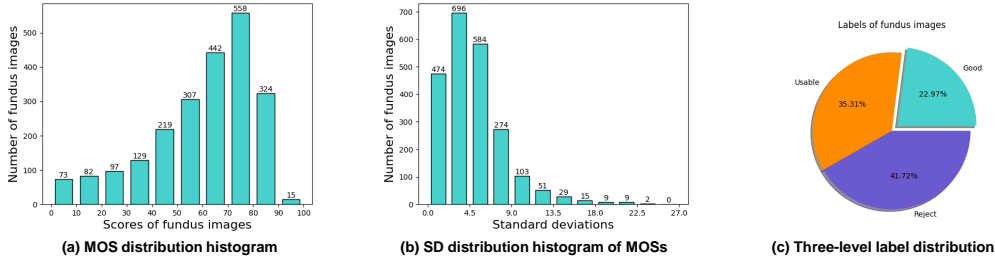


Figure 2: The statistic information of our FQS. (a) The MOS distribution histogram. Most of the MOSs are distributed between 60 and 80, which is consistent with actual clinical experience, and images of either extremely high or low quality are rare. (b) The standard deviation distribution histogram of MOSs. Half of the images have standard deviations under 4.34. Low SDs indicate that, though the opinion scores are given independently, the scoring criteria are consistent. (c) The three-level label distribution. The numbers of ‘Good’, ‘Usable’, and ‘Reject’ are 516, 793, and 937. There are more ‘Reject’ images to cover more degradation types.

“Usable”, and “Reject” are 516, 793, and 937, respectively. The distribution of the three-level classification label is consistent with the MOSs, which is common in actual clinical fundus image collecting.

Standard Deviation Distribution Histogram Since the MOS of each fundus image consists of multiple independent opinion scores from several ophthalmologists, it is necessary to evaluate the uniformity of these six scores. We calculate the standard deviation (SD) of each image and make the following SD distribution histogram (Fig. 2 (b)). About a quarter of the SDs are less than 2.52, half of the SDs are under 4.34, and three-quarters are under 6.37. Thus, the distribution of SD indicates the consistency of opinion scores and proves that prior knowledge of the labeling process is consistent between opinion givers.

2.2. method

2.2.1. Overall Architecture

The architecture of FTHNet is shown in Fig.3, which consists of 4 parts: the Transformer Backbone, the Distortion Perception Network, the Parameter Hypernetwork, and the Target Network.

The Transformer Backbone contains a patch embedding layer and four stages in different resolutions. Each stage comprises several Basic Transformer Blocks (BTBs) and a downsampling layer. **Firstly**, assuming an input fundus image, $\mathbf{I}_m \in \mathbb{R}^{H \times W \times 3}$, the Transformer Backbone exploits a non-overlapping patch embedding layer consisting of a 4×4 convolution (*conv*) to extract shallow feature $\mathbf{I}_0 \in \mathbb{R}^{\frac{H}{4} \times \frac{W}{4} \times C}$. **Secondly**, 4 stages are used for feature extraction on \mathbf{I}_0 . We adopt a 4×4 *conv* with stride 2 as the downsampling layer to the feature maps and double the channel dimension. Thus, the feature of the i -th stage is denoted as $\mathbf{X}_i \in \mathbb{R}^{\frac{H}{4 \times 2^i} \times \frac{W}{4 \times 2^i} \times 2^i C}$. Here, $i = 0, 1, 2, 3$ indicates the four stages.

We design the Distortion Perception Network to extract distorted information, as shown in Fig. 3(b). Each stage input is processed in the Distortion Perception Block (DPB). The input feature maps are $\mathbf{X}_i, i = 0, 1, 2, 3$. Then, we get four distorted information vectors through the DPB. Finally, distorted information vectors are concatenated to obtain the semantic vector $\mathbf{V} \in \mathbb{R}^{L \times 1}$.

The parameters of the Target Network are generated from the Parameter Hypernetwork shown in Fig.3(c). We design five stages for processing the parameters: one 1×1 *conv* layer for channel merging and one Parameter Generating Layer (PGL). The Parameter Hypernetwork gets input directly from the final stage of the Transformer Backbone. The input feature map is denoted as $\mathbf{X}_3 \in \mathbb{R}^{\frac{H}{32} \times \frac{W}{32} \times 8C}$. We adopt a 1×1 *conv* layer to merge channels by half. After channel merging, the feature of the i -th stage is denoted as $\mathbf{P}_i \in \mathbb{R}^{\frac{H}{32} \times \frac{W}{32} \times \frac{8C}{2^i}}$. Here, $i = 0, 1, 2, 3, 4$ indicates the five stages. Then, the Parameter Hypernetwork exploits the PGL to generate the weights and biases of the linear layers for the Target Network. The weights and bias are denoted as $\mathbf{W}\mathbf{P}_i$ and $\mathbf{B}\mathbf{P}_i$.

The Target Network consists of five linear layers. The input is the \mathbf{V} from the Distortion perception Network. The weights and biases of the Target Network are from the Parameter Hypernetwork. We utilize five linear layers to generate the predicted fundus image quality scores.

In the implementation, we change the patch embedding channel C and the combination (N_1, N_2, N_3, N_4) in the Transformer Backbone to establish two different FTHNet models: FTHNet-S: (2,4,6,2), $C:32$; FTHNet-L: (2,4,6,2), $C:64$.

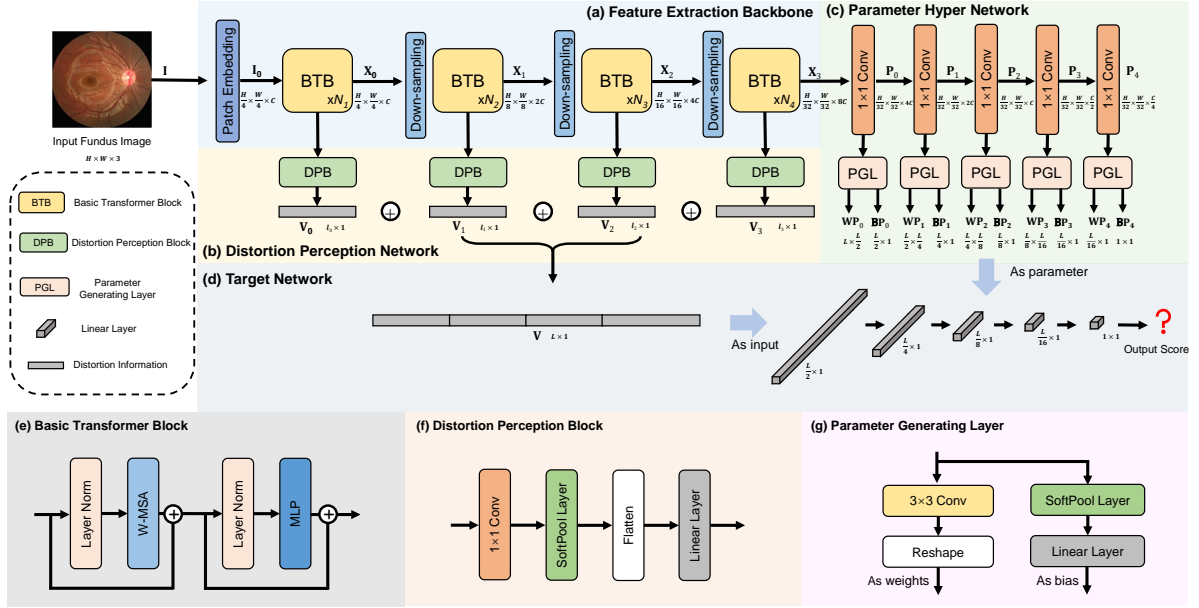


Figure 3: Architecture of our FTHNet. (a) The Transformer Backbone includes a patch embedding layer and four feature extraction stages. (b) The Distortion Perception Network is designed to extract distorted information. (c) The Parameter Hypernetwork comprises five parameter-generating layers. (d) The Target Network contains five linear layers to predict the fundus image quality scores. (e) The structure of the Basic Transformer Block. (f) The distortion perception block extracts the distortion information from the feature maps in different resolutions. (g) Each parameter-generating layer includes two branches to generate weight and bias parameters.

2.2.2. Basic Transformer Block

The emergence of Transformer provides an alternative to address the limitations of CNN-based methods in modeling non-local self-similarity and long-range dependencies. However, the computational cost of the standard global Transformer is quadratic to the spatial size of the input feature (HW). Therefore, to avoid this problem, we apply the transformer blocks with the Window-based Multi-head Self-Attention (W-MSA) [21] in the Transformer Backbone. The computational complexity of W-MSA is linear to the spatial size, which is more wieldable than standard global MSA. We also add the alternate window-shifting operation in the BTB to introduce cross-window connections. The BTB consists of one W-MSA, one Multilayer Perceptron (MLP), and two normalization layers, as shown in Fig. 3(e). BTB can be formulated as eq.2.

$$\begin{aligned} \mathbf{F}' &= \text{W-MSA}(\text{LN}(\mathbf{F}_{in})) + \mathbf{F}_{in}, \\ \mathbf{F}_{out} &= \text{MLP}(\text{LN}(\mathbf{F}')) + \mathbf{F}', \end{aligned} \quad (2)$$

where \mathbf{F}_{in} represents the input feature maps of a BTB. $\text{LN}(\cdot)$ represents the layer normalization. \mathbf{F}' and \mathbf{F}_{out} denote the output feature of W-MSA and MLP respectively.

where $\text{Concat}(\cdot)$ denotes the concatenating operation and $\mathbf{W}^O \in \mathbb{R}^{C \times C}$ are learnable parameters. We reshape \mathbf{X}_o^i to obtain the output window feature map $\mathbf{X}_{out}^i \in$

$\mathbb{R}^{L \times L \times C}$. Finally, we merge all the patch representations $\{\mathbf{X}_{out}^1, \mathbf{X}_{out}^2, \mathbf{X}_{out}^3, \dots, \mathbf{X}_{out}^N\}$ to obtain the output feature maps $\mathbf{X}_{out} \in \mathbb{R}^{H \times W \times C}$.

Multilayer Perception

The Multilayer Perception (MLP) in the BTB resembles the most utilized methods in Transformers, consisting of a linear layer with a GELU activation, two dropout layers, and another linear layer.

2.2.3. Distortion Perception Block

We design the DPB in the Distortion Perception Network to extract the distortion information from the feature maps in different resolutions. Distortions of the fundus images are widely distributed on different scales. For example, spots and flares affect only some small areas; over-darkness and over-exposure influence the whole image. Rather than dealing with the final feature map, the DPBs get inputs from four backbone stages in different resolutions.

As depicted in Fig. 3(f), the DPB consists of one 1×1 conv layer, one SoftPool [22] layer, and one linear layer. We adopt the 1×1 conv and SoftPool to merge the channels and to downscale the spatial size of feature maps, respectively. The DPB can be formulated as follows:

$$\begin{aligned} \mathbf{X}' &= \text{SoftPool}(1 \times 1 \text{ Conv}(\mathbf{X})), \\ \mathbf{V} &= \text{Linear}(\text{Flatten}(\mathbf{X}')), \end{aligned} \quad (3)$$

where $\mathbf{X} \in \mathbb{R}^{H \times W \times C}$ are the input feature map of a DPB. SoftPool, 1×1 Conv, Linear, and Flatten represents the SoftPool layer, the 1×1 conv layer, the linear layer, and flatten operation, respectively. $\mathbf{X}' \in \mathbb{R}^{\frac{H}{12} \times \frac{W}{12} \times \frac{C}{8}}$ denotes the output feature. $\mathbf{V} \in \mathbb{R}^{k \times 1}$ is the distortion information vector.

2.2.4. Parameter Generating Layer

The parameters of the Target Network are processed by the Parameter Generating Layer (PGL) shown in Fig. 3(g). The PGL consists of two branches, one for generating the weight parameters and another for generating the bias parameters. The weight branch is formulated as follows:

$$\mathbf{WP} = \text{Reshape}(3 \times 3 \text{ Conv}(\mathbf{P})) \quad (4)$$

Where \mathbf{P} denotes the input feature map of PGL. \mathbf{WP} represents the weight parameter. 3×3 Conv and Reshape represent the 3×3 conv layer and reshape operation respectively.

Similarly, the bias branch can be formulated as follows:

$$\mathbf{BP} = \text{Linear}(\text{SoftPool}(\mathbf{P})) \quad (5)$$

where \mathbf{BP} represents the weight parameter. Linear and SoftPool denote the linear layer and SoftPool layer respectively.

Though this process seems complicated, it can directly generate the parameter matrix with desired shape and length if we calculate the output channel using $\frac{\text{Channel}_{in} \times H \times W}{2^{l-1} \times \frac{L}{2^l}}$, where $H \times W$ represents the size of the feature map, and L represents the input length of Target Network in the i th stage.

2.2.5. Loss Function

We choose the smooth L1 loss[23] as our model's loss function. To be specific, the smooth L1 loss is formulated as

$$\mathcal{L}_{\text{smoothL1}} = \begin{cases} |y - y'| - 0.5, & \text{otherwise} \\ 0.5 \times (y - y')^2, & -1 < y - y' < 1 \end{cases} \quad (6)$$

where y denotes the ground-truth fundus image quality score, y' denotes the predicted score.

3. Results

3.1. Implementation Details

The train, test, and validation subsets are split proportionately 80%, 15%, and 5% randomly in each round, and 10-round cross-validation is applied in training.

During the training procedure, Fundus images are resized to 384×384 . The Adam [24] optimizer is adopted. We also apply data augmentation consisting of horizontal/vertical flip and random crop. The learning rate is set to 0.5×10^{-4} with linear annealing, and the batch size is set to 16. We use PyTorch 1.9 and CUDA 11.2. Every model is trained for 120000 iterations with a warming-up of 1000 iterations, equivalently 853 epochs. It takes about 12 hours to use an NVIDIA RTX3090 GPU to finish the training process.

We chose root mean square error (RMSE), Pearson correlation coefficient (PLCC), and Spearman's rank correlation coefficient (SRCC) as the metrics to evaluate the performance of our model.

The RMSE in eq. 7 shows the deviation between the prediction and target values. The lower the RMSE, the more robust the model in prediction.

$$RMSE = \sqrt{\frac{1}{n} \sum_{i=1}^n (y'_i - y_i)^2} \quad (7)$$

where y_i denotes the ground-truth MOS, y'_i denotes the predicted MOS.

The PLCC and SRCC are both standard metrics applied in the IQA works. The PLCC shown in eq.8 varies from -1 to 1 and shows the correlation between prediction and target values. The higher PLCC means the model's predictions are closer to the images' actual scores.

$$PLCC = \frac{\sum_i (y'_i - \bar{y}') (y_i - \bar{y})}{\sqrt{\sum_i (y'_i - \bar{y}')^2 \sum_i (y_i - \bar{y})^2}} \quad (8)$$

where \bar{y}' represents the average value of y'_i and \bar{y} represents the average value of y_i .

The SRCC in eq.9 varies from -1 to 1 and measures the monotonicity of the models' prediction.

$$SRCC = 1 - \frac{6 \sum_{i=1}^N d_i^2}{N(N^2 - 1)} \quad (9)$$

where $d_i = y'_i - y_i$ denotes the difference between y'_i and y_i .

3.2. Comparisons with State-of-the-Art Methods

We compare our FTHNet with several SOTA methods, including four model-based methods (BRISQUE[25], ILINIQUE[26], BIQI[27], and DIVINE[28]) and four deep learning methods (DeepIQA[12], HyperIQA[13], GraphIQA[14], and TRIQ[15]).

Table 1: Quantitative comparisons with SOTA algorithms on our FQS.

Method	SRCC	PLCC	RMSE	Params(M)
TRIQ [15]	0.4153	0.4327	-	23.68
DeepIQA [12]	0.2964	0.2798	-	6.29
HyperIQA [13]	0.9351	0.9305	-	28.28
GraphIQA [14]	0.9280	0.9355	-	51.52
BRISQUE [25]	0.9020	0.9220	8.039	-
ILINIQE [26]	0.6550	0.7191	35.46	-
BIQI [27]	0.5788	0.5492	76.2	-
DIVINE [28]	0.1566	0.1686	43.19	-
FTHNet-S (Ours)	0.9330	0.9435	7.118	5.662
FTHNet-L (Ours)	0.9358	0.9442	7.024	14.88

As shown in the Tabel.1, The model-based methods mentioned above can merely reach the performance of FTHNet, though these methods are retrained on our FQS dataset. Since the model-based methods do not have network parameters and computing flops, the corresponding data is not shown in the table.

The IQA methods had not been applied to FIQA tasks before this work, and we retrained HyperIQA, GraphIQA, and TRIQ for their best performance in the comparison study. The quantitative comparisons on our FQS dataset are shown in Table.1. Our best model, FTHNet-L, achieves 0.0133, 0.0183, 0.5161, and 0.6690 improvements in PLCC compared to GraphIQA, HyperIQA, TRIQ, and DeepIQA. Meanwhile, FTHNet-L has 0.0143, 0.0072, 0.5270, and 0.6459 better performance in SRCC, respectively. These improvements of FTHNet-L are significant enough for IQA tasks.

Furthermore, although FTHNet-L is already smaller than most other models, our lightweight model, FTHNet-S, outperforms other methods by 0.008, 0.013, 0.5108, and 0.6637 in PLCC, respectively, while requiring 5.67 M Params.

3.3. Ablation Study

3.3.1. Transformer Backbone

To analyze the effect of the Transformer Backbone, we compare our BTB with three solid Transformer Backbones in Table. 2, including two CNN-based backbones (ResNet[32] and ConvNeXt[30]) and one Transformer-based backbone(MSG-Transformer[31]) with other structure of FTHNet unchanged. It can be observed in the table that our proposed BTB achieves the best performance.

3.3.2. Window Shift Operations

The window shift operations are designed to augment the information exchange between adjacent windows in the BTBs. We conducted the ablation study to analyze

the effect of the window shift operations. The results are reported in Table. 2. The results indicate that the window shift operations can build cross-window connections and improve the performance of FTHNet.

3.3.3. Depth and Patch Embedding Channel

We explore the effect of different patch embedding channels C and combinations (N_1, N_2, N_3, N_4) in the extraction backbone on model performance after choosing the BTB with W-MSA as the extraction block. The results are shown in Table. 3.

It can be observed that our FTHNet-L $((2, 2, 6, 2), C:64)$ can achieve the best performance. Compared with other patch embedding channels, 64 is the optimal choice. Considering the performance and model parameters, we finally chose $((2, 4, 6, 2), C:32)$ as our FTHNet-S.

3.3.4. Downsampling Structure

We conduct this ablation study to explore the effect of downsampling structure in the Parameter Hypernetwork. Two downsampling structures are available in the Parameter Hypernetwork: stepwise and direct downsampling. As shown in Table. 2, compared with the direct structure, the stepwise downsampling structure achieves almost the same performance with fewer model parameters and computational complexity. Thus, we choose the stepwise downsampling structure in our FTHNet.

3.3.5. Loss Function

We test different loss functions, including L1 loss, L2 loss, and Smooth L1 loss[23], while training the models for better performance. The L1 loss is the most common function in the IQA. In addition, L2 loss and Smooth L1 loss are also applied in the IQA.

As listed in Table.2, compared with other loss functions, Smooth L1 loss achieves the best performance in PLCC and RMSE. Meanwhile, Smooth L1 loss gets the second-best performance in SRCC. Thus, we choose the Smooth L1 loss as the loss function of our FTHNet.

4. Discussion

4.1. Deployment Experiment

We deploy our FTHNet as an Application Program Interface (API) on a GPU server and bind our FTHNet with a new automatic diagnosis system. This system can process fundus images and provide ophthalmologists with pathology information and the reliability of images. If the score of one image is high, the pathology

Table 2: Ablation study of Transformer Backbone, window shifted operation(WSO), loss function, downsampling structure, and hypernetwork structure.

Type	Method	SRCC	PLCC	RMSE	Params(M)	FLOPS
Backbones	ResNet[29]	0.1672	0.1630	39.24	27.97	12.70 G
	ConvNeXt-L[30]	0.8095	0.8081	12.19	55.25	26.30 G
	MSG Transformer[31]	0.9241	0.9277	7.615	33.29	16.02 G
	BTB	0.9358	0.9442	7.024	14.88	6.044 G
WSO	w/o	0.9263	0.9405	7.356	14.88	6.044 G
	with	0.9358	0.9442	7.024	14.88	6.044 G
Loss	\mathcal{L}_1	0.93245	0.9439	6.716	14.88	6.044 G
	\mathcal{L}_2	0.9363	0.9389	7.028	14.88	6.044 G
	$\mathcal{L}_1 + \mathcal{L}_2$	0.93405	0.9408	6.914	14.88	6.044 G
	$\mathcal{L}_{smoothL1}$	0.9345	0.9447	6.581	14.88	6.044 G
Downsampling Structure	Direct	0.9357	0.9426	6.978	0.572	82.39 M
	Stepwise	0.9354	0.9437	6.988	0.393	56.67 M
hypernetwork	w/o	0.6092	0.6077	20.93	12.28	5.06 G
	with	0.9358	0.9442	7.024	14.88	6.044 G

Table 3: Ablation study of combination (N_1, N_2, N_3, N_4) and patch embedding channel(C)

(N_1, N_2, N_3, N_4)	C	SRCC	PLCC	RMSE	Params(M)
(2, 2, 2, 2)	32	0.9328	0.9409	7.328	4.748
(2, 2, 2, 2)	64	0.9355	0.9418	7.127	11.70
(2, 2, 6, 2)	32	0.9331	0.9439	7.094	5.558
(2, 2, 6, 2)	64	0.9358	0.9442	7.024	14.88
(2, 2, 6, 2)	96	0.9332	0.9404	7.156	30.34
(2, 4, 6, 2)	32	0.9303	0.9424	7.161	5.662
(2, 4, 6, 2)	64	0.9338	0.9437	6.962	15.28
(2, 4, 6, 2)	96	0.9312	0.9430	6.971	31.23
(2, 2, 12, 2)	64	0.9323	0.9415	7.112	19.64
(2, 2, 12, 2)	96	0.9279	0.9395	7.039	41.02
(2, 2, 18, 2)	64	0.9356	0.9416	7.266	24.40
(2, 2, 18, 2)	96	0.9314	0.9374	7.2975	51.71

information distinguished by the system shall be more trustworthy. The ophthalmologists utilizing this system can choose how to use the result based on the score of the FTHNet.

The screenshot displays the FTHNet diagnosis system interface. It is divided into two main sections: '患病风险' (Disease Risk) and '分析结果' (Analysis Result).
 Under '患病风险', there are two tables:
 1. '糖尿病视网膜病变' (Diabetic Retinopathy): A table with '可能患病' (Possible disease) and '正常' (Normal).
 2. '青光眼' (Glaucoma): A table with '可能患病' (Possible disease) and '正常' (Normal).
 Under '分析结果', there are two tables:
 1. 'Risks': A table with 'DR' (Diabetic Retinopathy) and 'Glaucoma'. The DR status is 'Risky' and Glaucoma is 'Normal'.
 2. 'Analysis Result': A table showing 'Image Quality: Usable, score 59/100'. Below it, a text box contains: 'Lesion Description: Suspected fundus disease; Hard exudation, Haemorrhage, Microhemangioma, Soft exudation. Disease Risks: DR 100%, Non-proliferative risk 64.5%,.....'.
 Red boxes highlight the 'Image Quality' score and the 'Disease Risks' text in the analysis result section.

Figure 4: Implementation of the FTHNet in the diagnosis system. The FTHNet works in the emphasized region.

Table 4: Evaluation time consumption of different FTHNet models.

Methods	Params(M)	FLOPS(G)	Single Test(ms)
FTHNet-S	5.662	1.981	44.45
FTHNet-L	14.88	6.044	56.31

4.2. Potential of Real-time assessment

The inference speed is one of the most critical factors affecting the application of our FTHNet in clinical diagnosis. We deploy our FTHNet as an API on a GPU server to test the inference time of our FTHNet, and the results are in Table.4. The single test means the average inference time of a single fundus image.

We can observe from Table.4 that the inference time of FTHNet-S is 44.45 ms, and even FTHNet-L is only 56.31 ms. With the short inference time, our FTHNet can provide real-time assessment in clinical diagnosis.

4.3. Effect of hypernetwork Structure

In this subsection, we discuss the effect of the hypernetwork structure on FIQA tasks.

To explore the importance of hypernetwork structure in the FIQA task, we conduct this experiment and show the results in Table.2. Note that *w/o hyper network* means the parameters of the Target Network are learned by backpropagation rather than provided by the hypernetwork.

It can be observed that the performance of FTHNet improves significantly with hypernetwork structure despite a slight increase in model parameters. It indicates

Fundus Images				
Predict	20.92	7.90	34.29	33.99
GT	46.89	28.67	12.89	52.77

Figure 5: Failed cases of FTHNet on our FQS dataset. Most of these failed cases are from the "Reject" category. The FTHNet and FQS dataset will be refined according to these failed cases.

the importance of hypernetwork structure in the FIQA tasks. Our FTHNet is constructed based on the hypernetwork structure. The Target Network has flexible parameters from the hypernetwork varying with the input image, which is essential for the quality assessment with fundus images of complex and diverse degradation.

4.4. Fail cases

Although FTHNet achieves good performance, it may not work in some scenes. Fig.5 shows some failed cases of FTHNet on our FQS dataset. As shown in Fig.5, there is a wide gap between the predicted MOSs and the ground truth. Further observation reveals that the three-level classification labels of these failed cases are all "Reject". Furthermore, the degradation types are mainly a combination of severe blur and haze, with few samples in our FQS dataset. Though the prediction keeps them in the correct category, it shows that the number of samples limits the performance of our FTHNet in determining the scores for these images. We will continue to enrich and improve our FQS dataset according to these failed cases.

5. Conclusions

Traditional FIQA methods: most give classification prediction; it is difficult to compare results within each category; algorithms are old and not deployed in practice.

Our FTHNet: It is trained to give continuous quality scores, which are intuitive and convenient to compare; it is lightweight and easy to deploy in automatic diagnosis systems; it has a new transformer-based hypernetwork architecture and leading performance among IQA methods.

We will release codes of the FTHNet and full details of the FQS dataset for further research. Meanwhile, we are also willing to offer fundus image dataset-building tools for other fundus image research. We hope this work can serve as a baseline for FIQA and benefit the

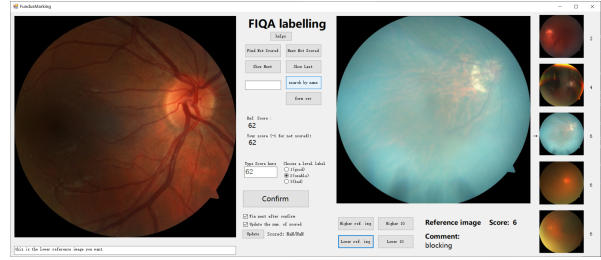


Figure A.6: The User Interface of our assistive labeling application, the FundusMarking. The FundusMarking is convenient and useful for inexperienced and experienced users, allowing ophthalmologists to provide normative source data easily.

fundus image research by providing a new quantitative metric in the future.

CRediT authorship contribution statement

Zheng Gong: Conceptualization, Methodology, Software, Validation, Data Curation, Writing - Original Draft, Visualization. **Zhuo Deng:** Methodology, Software, Validation, Data Curation, Writing - Original Draft, Visualization. **Run Gan:** Conceptualization, Data Curation, Writing - Review and Editing. **Zhiyuan Niu:** Data Curation, Validation, Writing - Review and Editing. **Weihao Gao:** Validation, Writing - Review and Editing. **Lu Chen:** Data Curation, Project administration. **Canfeng Huang:** Data Curation. **Jia Liang:** Data Curation. **Fang Li:** Project administration. **Shaochong Zhang:** Funding acquisition. **Lan Ma:** Funding acquisition.

Acknowledgments

This work was supported by the Project from the Science and Technology Innovation Committee of Shenzhen-Platform and Carrier (International Science and Technology Information Center) and Shenzhen Bay Lab [KCXFZ20211020163813019]. This work involved human subjects in its research. Approval of all ethical and experimental procedures and protocols was granted by the Shenzhen Eye Hospital under the ETHICAL NUMBER 2022KYPJ062.

Appendix A. FundusMarking

Fig. A.6 shows the User Interface of our assistive labeling application (FundusMarking).

Appendix B. Downsampling structure in Parameter Hypernetwork

As shown in Fig. B.7(b), the direct downsampling of each stage gets the same input feature map X_3 from the final BTB. In Fig. B.7(a), the stepwise downsampling of

Table B.5: The theoretical parameters and computation of downsampling structure in Parameter Hypernetwork.

Structure	Layer	Params	FLOPS
Direct	1	$\frac{1}{3} \times C^2 \times K^2$	$\frac{1}{3} \times C^2 \times K^2 Map^2$
Direct	2	$\frac{1}{4} \times C^2 \times K^2$	$\frac{1}{4} \times C^2 \times K^2 Map^2$
Direct	3	$\frac{1}{8} \times C^2 \times K^2$	$\frac{1}{8} \times C^2 \times K^2 Map^2$
Direct	4	$\frac{1}{16} \times C^2 \times K^2$	$\frac{1}{16} \times C^2 \times K^2 Map^2$
Stepwise	1	$\frac{1}{3} \times C^2 \times K^2$	$\frac{1}{3} \times C^2 \times K^2 Map^2$
Stepwise	2	$\frac{1}{4} \times C^2 \times K^2$	$\frac{1}{4} \times C^2 \times K^2 Map^2$
Stepwise	3	$\frac{1}{8} \times C^2 \times K^2$	$\frac{1}{8} \times C^2 \times K^2 Map^2$
Stepwise	4	$\frac{1}{128} \times C^2 \times K^2$	$\frac{1}{128} \times C^2 \times K^2 Map^2$

each stage gets its input feature map from the previous downsampling layer, which utilizes the previous 1×1 convolution layer to reduce the parameters and computation.

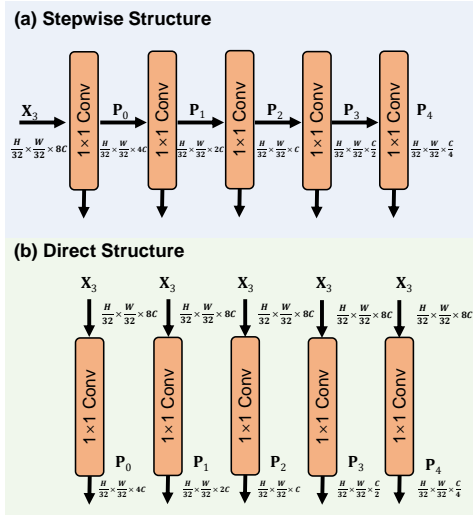


Figure B.7: The architecture of downsampling structure in Parameter Hypernetwork. (a) stepwise downsampling structure. (b) direct structure.

Fig. B.7 shows the two different architectures of downsampling structure in Parameter Hypernetwork. Table. B.5 shows the theoretical parameters and computation of the downsampling structure in the Parameter Hypernetwork.

References

- [1] S. Majumder, N. Kehtarnavaz, Multitasking deep learning model for detection of five stages of diabetic retinopathy, arXiv preprint arXiv:2103.04207.
- [2] C.-H. Hua, K. Kim, T. Huynh-The, J. I. You, S.-Y. Yu, T. Le-Tien, S.-H. Bae, S. Lee, Convolutional network with twofold feature augmentation for diabetic retinopathy recognition from

multi-modal images, IEEE Journal of Biomedical and Health Informatics.

- [3] Y. Peng, S. Dharssi, Q. Chen, T. D. Keenan, E. Agrón, W. T. Wong, E. Y. Chew, Z. Lu, Deepseenet: a deep learning model for automated classification of patient-based age-related macular degeneration severity from color fundus photographs, *Ophthalmology* 126 (4) (2019) 565–575.
- [4] P. Burlina, D. E. Freund, N. Joshi, Y. Wolfson, N. M. Bressler, Detection of age-related macular degeneration via deep learning, in: 2016 IEEE 13th International Symposium on Biomedical Imaging (ISBI), IEEE, 2016, pp. 184–188.
- [5] C. M. G. Cheung, T. Y. Lai, P. Ruamviboonsuk, S.-J. Chen, Y. Chen, K. B. Freund, F. Gomi, A. H. Koh, W.-K. Lee, T. Y. Wong, Polypoidal choroidal vasculopathy: definition, pathogenesis, diagnosis, and management, *Ophthalmology* 125 (5) (2018) 708–724.
- [6] N. Mojab, V. Noroozi, S. Y. Philip, J. A. Hallak, Deep multi-task learning for interpretable glaucoma detection, in: 2019 IEEE 20th International Conference on Information Reuse and Integration for Data Science (IRI), IEEE, 2019, pp. 167–174.
- [7] W. Liao, B. Zou, R. Zhao, Y. Chen, Z. He, M. Zhou, Clinical interpretable deep learning model for glaucoma diagnosis, *IEEE journal of biomedical and health informatics* 24 (5) (2019) 1405–1412.
- [8] S. Philip, L. Cowie, J. Olson, The impact of the health technology board for scotland’s grading model on referrals to ophthalmology services, *British Journal of Ophthalmology* 89 (7) (2005) 891–896.
- [9] S. C. Lee, Y. Wang, Automatic retinal image quality assessment and enhancement, in: *Medical imaging 1999: image processing*, Vol. 3661, SPIE, 1999, pp. 1581–1590.
- [10] M. Lalonde, L. Gagnon, M.-C. Boucher, et al., Automatic visual quality assessment in optical fundus images, in: *Proceedings of vision interface*, Vol. 32, Ottawa, 2001, pp. 259–264.
- [11] T. Köhler, A. Budai, M. F. Kraus, J. Odstrčilik, G. Michelson, J. Hornegger, Automatic no-reference quality assessment for retinal fundus images using vessel segmentation, in: *Proceedings of the 26th IEEE international symposium on computer-based medical systems*, IEEE, 2013, pp. 95–100.
- [12] S. Bosse, D. Maniry, K.-R. Müller, T. Wiegand, W. Samek, Deep neural networks for no-reference and full-reference image quality assessment, *IEEE Transactions on Image Processing* 27 (1) (2018) 206–219. doi:10.1109/TIP.2017.2760518.
- [13] S. Su, Q. Yan, Y. Zhu, C. Zhang, X. Ge, J. Sun, Y. Zhang, Blindly assess image quality in the wild guided by a self-adaptive hyper network, in: *Proceedings of the IEEE/CVF Conference on Computer Vision and Pattern Recognition*, 2020, pp. 3667–3676.
- [14] S. Sun, T. Yu, J. Xu, W. Zhou, Z. Chen, Graphiqa: Learning distortion graph representations for blind image quality assessment, *IEEE Transactions on Multimedia*.
- [15] J. You, J. Korhonen, Transformer for image quality assessment, in: 2021 IEEE International Conference on Image Processing (ICIP), 2021, pp. 1389–1393. doi:10.1109/ICIP42928.2021.9506075.
- [16] H. Fu, B. Wang, J. Shen, S. Cui, Y. Xu, J. Liu, L. Shao, Evaluation of retinal image quality assessment networks in different color-spaces, in: D. Shen, T. Liu, T. M. Peters, L. H. Staib, C. Essert, S. Zhou, P.-T. Yap, A. Khan (Eds.), *Medical Image Computing and Computer Assisted Intervention – MICCAI 2019*, Springer International Publishing, Cham, 2019, pp. 48–56.
- [17] Y. Shen, R. Fang, B. Sheng, L. Dai, H. Li, J. Qin, Q. Wu, W. Jia, Multi-task fundus image quality assessment via transfer learning and landmarks detection, in: *International Workshop on Ma-*

- chine Learning in Medical Imaging, Springer, 2018, pp. 28–36.
- [18] A. Vaswani, N. Shazeer, N. Parmar, J. Uszkoreit, L. Jones, A. N. Gomez, Ł. Kaiser, I. Polosukhin, Attention is all you need, in: *Advances in neural information processing systems*, 2017, pp. 5998–6008.
 - [19] A. Raj, A. K. Tiwari, M. G. Martini, Fundus image quality assessment: survey, challenges, and future scope, *IET Image Processing* 13 (8) (2019) 1211–1224.
 - [20] R. W. Strauss, T. R. Krieglstein, S. G. Priglinger, W. Reis, M. W. Ulbig, A. Kampik, A. S. Neubauer, Image quality characteristics of a novel colour scanning digital ophthalmoscope (sdo) compared with fundus photography, *Ophthalmic and Physiological Optics* 27 (6) (2007) 611–618.
 - [21] Z. Liu, Y. Lin, Y. Cao, H. Hu, Y. Wei, Z. Zhang, S. Lin, B. Guo, Swin transformer: Hierarchical vision transformer using shifted windows, *arXiv preprint arXiv:2103.14030*.
 - [22] A. Stergiou, R. Poppe, G. Kalliatakis, Refining activation downsampling with softpool, in: *Proceedings of the IEEE/CVF International Conference on Computer Vision*, 2021, pp. 10357–10366.
 - [23] R. Girshick, Fast r-cnn, in: *2015 IEEE International Conference on Computer Vision (ICCV)*, 2015, pp. 1440–1448. doi:10.1109/ICCV.2015.169.
 - [24] D. P. Kingma, J. Ba, Adam: A method for stochastic optimization, *arXiv preprint arXiv:1412.6980*.
 - [25] A. Mittal, A. K. Moorthy, A. C. Bovik, No-reference image quality assessment in the spatial domain, *IEEE Transactions on Image Processing* 21 (12) (2012) 4695–4708. doi:10.1109/TIP.2012.2214050.
 - [26] L. Zhang, L. Zhang, A. C. Bovik, A feature-enriched completely blind image quality evaluator, *IEEE Transactions on Image Processing* 24 (8) (2015) 2579–2591. doi:10.1109/TIP.2015.2426416.
 - [27] A. K. Moorthy, A. C. Bovik, A two-step framework for constructing blind image quality indices, *IEEE Signal Processing Letters* 17 (5) (2010) 513–516. doi:10.1109/LSP.2010.2043888.
 - [28] A. K. Moorthy, A. C. Bovik, Blind image quality assessment: From natural scene statistics to perceptual quality, *IEEE Transactions on Image Processing* 20 (12) (2011) 3350–3364. doi:10.1109/TIP.2011.2147325.
 - [29] K. He, X. Zhang, S. Ren, J. Sun, Deep residual learning for image recognition, in: *Proceedings of the IEEE conference on computer vision and pattern recognition*, 2016, pp. 770–778.
 - [30] Z. Liu, H. Mao, C.-Y. Wu, C. Feichtenhofer, T. Darrell, S. Xie, A convnet for the 2020s, *Proceedings of the IEEE/CVF Conference on Computer Vision and Pattern Recognition (CVPR)*.
 - [31] J. Fang, L. Xie, X. Wang, X. Zhang, W. Liu, Q. Tian, Msg-transformer: Exchanging local spatial information by manipulating messenger tokens, in: *CVPR*, 2022.
 - [32] K. He, X. Zhang, S. Ren, J. Sun, Deep residual learning for image recognition, in: *2016 IEEE Conference on Computer Vision and Pattern Recognition (CVPR)*, 2016, pp. 770–778. doi:10.1109/CVPR.2016.90.